steel research international
www.steel-research.de

Dynamic and Static Strain Aging in a High-Manganese Steel

Sebastian Wesselmecking, Wenwen Song, and Wolfgang Bleck*

Carbon-containing high-manganese steels are susceptible to strain aging, which influences the mechanical properties during and after deformation. To understand the strain aging behavior of austenitic Fe-22Mn-1.3Al-0.3C high-manganese steel, dynamic as well as static strain aging are examined. Dynamic strain aging, occurring during deformation, is quantified by tensile tests at different strain rates. The strain localization during straining is analyzed by digital image correlation. A decrease in strain rate increases the tensile strength and influences the onset of a serrated flow. Static strain aging is quantified by interrupted tensile tests, combined with digital image correlation and small-angle neutron scattering (SANS). The yield strength increases due to static strain aging at room temperature within the period of days. The samples show extended yield point (yield point elongation) and the effect strengthens at higher pre-deformation. With SANS, evidence of carbon-manganese ordering (C–Mn ordering) during aging is obtained and correlated.

1. Introduction

Austenitic high-manganese steels show outstanding properties such as high strain hardening, high energy absorption, and high ductility.[1–3] Therefore, high-manganese steels are promising next-generation structural materials in automotive and aerospace industries.[4–7] The high ductility is in particular based on their deformation mechanisms: transformation-induced plasticity (TRIP) and twinning-induced plasticity (TWIP).[8] TWIP results in a superior combination of strength and ductility depending on stacking fault energy, grain size, and chemical composition of the austenite phase.[1,9–11] Time-dependent effects are less in the focus of investigations but are known to have a strong influence on the deformation—like strain aging.[12,13] The conditions for strain aging are often interstitial elements such as carbon interacting with dislocations or point defects.[14–17] Strain aging has to be distinguished between dynamic strain aging and static strain aging.[18,19]

Static strain aging appears after deformation and is influenced by the aging time and the applied deformation.[20–22] In ferritic steels, it is used specifically to increase the yield strength (YS) of sheet material by a heat treatment integrated into paint lines. This so-called bake hardening utilizes the Cottrell effect and requires a previously applied small deformation and a temperature that allows diffusive processes of the interstitially dissolved carbon.[23,24] The Cottrell effect is a long-range diffusion-controlled mechanism. In contrast to ferritic body centered cubic (bcc) structures, the diffusion rate in austenitic face centered cubic (fcc) is 10–100 times lower.[25–27] In addition, even if carbon atoms are in the vicinity of dislocations, the isotropic stress field of the carbon atoms in octahedral sites is much smaller in fcc than in bcc, reducing the possible pinning-effect of dislocations, making the effect negotiable.[28]

A carbon-manganese ordering (C–Mn ordering) phenomena is reported to be responsible for strain aging in austenitic high-manganese steels.[12,29,30] Deformation in fcc steels comes along with shear on (111) planes, which is described to initiate a C–Mn ordering process.[12,31] Thereby, the carbon atom is displaced from an octahedral interstitial site into an energetically less favorable tetrahedral interstitial site in the crystal lattice.[12] The low activation energy, which is necessary for repositioning, increases the probability for a jump from a tetrahedral interstitial site into an octahedral site even at RT. This repositioning of carbon is expected into the energetically most favorable position, which is the octahedral interstitial site, surrounded by as many manganese atoms as possible.[12,32,33] This C–Mn ordering evokes three important changes: 1) an energetic minimization and thus a locally thermodynamically more stable system which promotes planar slip,[34] 2) locally enriched carbon and manganese contents and consequently local changes of SFE,[35] and 3) a proportionally stronger pinning of trailing partials increasing twinning.[36]

Understanding the processes that take place during strain aging and knowledge of the interaction of C–Mn ordering are important to control the mechanical properties and to facilitate industrial applicability.[5] Nevertheless, so far it is not possible to establish a clear connection between the formation of C–Mn ordering and the strain aging-related change in mechanical properties. In addition, while publications describe the influence of

S. Wesselmecking, W. Song, W. Bleck
IEHK Steel Institute
RWTH Aachen University
Aachen D-52072, Germany
E-mail: wesselmecking@iehk.rwth-aachen.de

The ORCID identification number(s) for the author(s) of this article can be found under https://doi.org/10.1002/srin.202100707.

DOI: 10.1002/srin.202100707

pre-deformation on the formation of a short-range order, the influence of rapid aging at room temperature is neglected. To obtain a comprehensive description, we investigate static and dynamic strain aging on one material. By using digital image correlation, we quantify and describe the aging-controlled, inhomogeneous deformation behavior during dynamic strain aging (serrated flow) and during static strain aging (pronounced yielding). To determine the correlation among increase in stress, change in deformation behavior, and short-range ordering, we investigate precisely the change in the mechanical properties, the forming behavior and the formation of short-range structures by small-angle neutron scattering (SANS).

2. Experimental Section

To describe the kinetics of static and dynamic strain aging in high-manganese steel, the Fe-22Mn-1.3Al-0.3C alloy is investigated. Tensile tests were conducted and strain localization during testing was examined by digital image correlation. The kinetics of static strain aging were analyzed by correlating results from interrupted tensile tests with results from SANS.

The high-manganese steel with the chemical composition as listed in **Table 1** was vacuum-melted and ingot casted. The ingot material with the dimensions of $140 \times 140\,mm^2$ was forged to the dimension of $120 \times 160\,mm^2$ at 1150 °C. Subsequently, a homogenization heat treatment was performed at 1180 °C for 4 h. The homogenized ingot was hot-rolled at 1150 °C to a plate thickness of 3 mm in several passes. Cold-rolling to 1.5 mm was performed and the sheets were recrystallized at 700 °C for 60 min in a salt bath with an inhibitor to avoid nitrogenization. The recrystallized material had an average grain size of 5.3 µm.

Sub-size tensile specimens with an initial gauge length of 25 mm according to DIN EN ISO 6892 were extracted by water cutting transverse to the rolling direction. A Zwick sample preparation machine was used to grind the edges and precisely adjust the parallel width. For the tensile tests, a Zwick Z250 universal tensile testing machine was used. The parallel length of the samples was coated with acryl-based spray paint (white on black) to measure the strain by digital image correlation. It was used to describe the inhomogeneous deformation behavior occurring during plastic deformation and especially to characterize the local deformation during yielding. A GOM Aramis (Gom software version 6.3) equipped with a Toshiba Teli CleverDragon 12 MP camera (and a lens with 50 mm focal length) was used. The analysis of the flat specimen was realized by a 2D setup at a grid size of $0.15\,mm^2$ at 16×16 pixels per facet and an overlap of 20%. A linear strain calculation with a magnitude of 3 and a validity rate of 55% was applied. The region of interest was 25 mm (203 pixels) in length and 6 mm (35 pixels) in width. The system was calibrated with the help of a coded plate, the calibration deviation was 0.0023 pixel and the scale deviation was 0.00 mm. To analyze static strain aging, the tensile tests were interrupted after defined plastic deformations of 20% and 50%. Samples were aged at room temperature for specific times (no aging, 3 days, 5 days). Aging was followed by tensile tests until failure. Due to the limited amount of material, only one test per condition was carried out.

Table 1. Chemical composition of the investigated TWIP steel Fe-22Mn-1.3Al-0.3C in wt%.

C	Mn	Si	P	S	Cr	Al	Fe
0.33	21.9	0.05	0.010	0.003	0.03	1.30	Balance

The aged samples of dimension $8 \times 1\,mm^2$ were analyzed by SANS at the beamline KWS-2 of the Jülich Centre for Neutron Science (JCNS) at the Heinz Maier-Leibnitz Zentrum (MLZ), Garching, Germany. With a neutron beam wavelength of $\lambda = 5$ Å, measurements were made at two detection distances, 1.74 m for the high Q region and 7.74 m for the low Q region. The collimation length was 8 m. The samples were measured in a 2.2 T transverse magnetic field to the beam axis achieved with an electromagnet. The evaluation was conducted using the software SASfit which is described elsewhere.[37]

3. Results

Dynamic strain aging of the Fe-22Mn-1.3Al-0.3C was analyzed at room temperature at strain rates of $5 \times 10^{-6}\,s^{-1}$, $2 \times 10^{-5}\,s^{-1}$, $1 \times 10^{-4}\,s^{-1}$, $1 \times 10^{-3}\,s^{-1}$, $2.5 \times 10^{-3}\,s^{-1}$, and $1 \times 10^{-2}\,s^{-1}$ (**Figure 1**a). The according, ultimate tensile strength (UTS), and total elongation (TE) values are given in **Table 2**. The TE possesses a certain scattering and ranges from 56 % to 66 %. The YS is not affected by the change in strain rate. The UTS decreases with increasing strain rate from 961 MPa ($5 \times 10^{-5}\,s^{-1}$) to 859 MPa ($1 \times 10^{-1}\,s^{-1}$) by ≈100 MPa. In this context, the decrease in tensile strength occurs linearly with a certain spread, if the strain rate is plotted logarithmically (Figure 1b). Thus, the strain rate sensitivity coefficient "m" of the extended Hollomon equation (Equation (1)) is negative.

$$\sigma_t = k * \varphi^n * \dot{\varphi}^m \tag{1}$$

($\boldsymbol{\sigma_t}$ is the true stress, **k** the Hollomon constant, **φ** the logarithmic strain, **n** the strain hardening exponent, and **m** the strain rate sensitivity coefficient.) The occurrence of serrated flow was recorded by means of digital image correlation and further analyzed. Strain localization was defined as a local strain rate increase, which is ≥5 times the global strain rate. The example shown in Figure 1c depicts the strain rate distribution at a strain rate of $2.5 \times 10^{-3}\,s^{-1}$, where the onset of strain localization is identified at a critical strain (ε_{krit}) of ≈41.5% global engineering strain. The values of ε_{krit} for all strain rates are depicted in Figure 1d. At a strain rate of $1 \times 10^{-3}\,s^{-1}$, the strain localization is observed at 40% of strain, while occurring at higher global strain for higher and lower strain rates. A tendency regarding the strength of strain localization from digital image correlation as a function of strain rate is not observed.

To determine **static strain aging**, tensile tests at $2.5 \times 10^{-3}\,s^{-1}$, (Figure 1a) green line) were interrupted at engineering strains of 20% and 50%. After the material was pre-deformed, it was further tested immediately after unloading. For comparison and investigation of static strain aging, tensile tests were carried out 3 and 5 days after pre-deformation as well. YS [$R_{P0.2}$ (YS during continuous yielding), R_e (YS during discontinuous yielding)], and UTS are listed in **Table 3**, the associated stress–strain curves

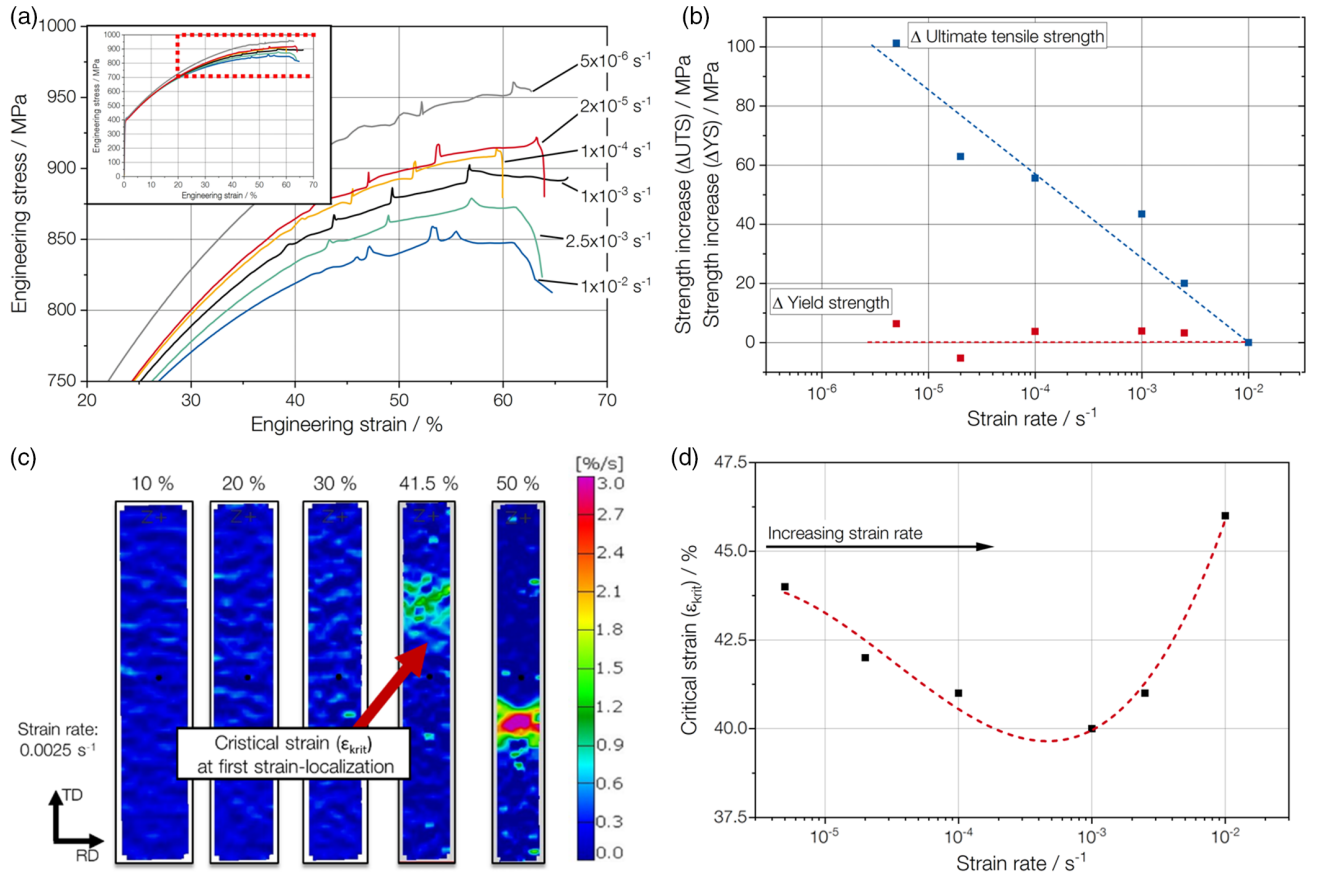

Figure 1. a) Stress–strain curves at different strain rates with a magnification of the region showing dynamic strain aging; b) Strain rate related change of YS and UTS; c) Local longitudinal strain rate, from digital image correlation at a global strain rate of $2.5 \times 10^{-3}\ s^{-1}$; d) Critical strains ($\varepsilon_{krit}$) of the investigated strain rates.

Table 2. Mechanical properties (YS, UTS, and TE) at different strain rates.

Strain rate [s^{-1}]	YS ($R_{P0.2}$) [MPa]	UTS [MPa]	TE [%]
5×10^{-6}	395	961	62.7
2×10^{-5}	389	922	63.9
1×10^{-4}	392	915	57.7
1×10^{-3}	392	902	66.2
2.5×10^{-3}	392	879	63.7
1×10^{-2}	389	859	55.7

Table 3. Mechanical properties at different times of room temperature aging.

Pre-deformation [%]	Aging Time [–]	YS ($R_{P0.2}$) [MPa]	YS (R_e) [MPa]	UTS [MPa]	TE [%]	$\Delta\varepsilon$ [%]
0%	Initial state	392	–	879	63.7	–
20%	Immediate	–	744	1028	49.3	0.1
20%	3 days	–	763	1054	49.1	0.7
20%	5 days	–	769	1064	48.6	1.3
50%	Immediate	–	1164	1251	23.8	2.6
50%	3 days	–	1186	1269	20.8	3.2
50%	5 days	–	1196	1271	17.9	2.6

are depicted in **Figure 2**a. Static strain aging after 20 % of elongation increases the YS by 19 and 25 MPa after 3 and 5 days, respectively. A higher pre-deformation of 50% had a greater effect on the change of YS, 20 MPa, and 30 MPa after 3 and 5 days, respectively. The stress increase (ΔYS) depicted in Figure 2b is accommodated by a pronounced yielding, which was found in all samples after aging. The first Lüders band propagation was analyzed by digital image correlation as depicted in Figure 2c, the corresponding local strain-shift $\Delta\varepsilon$ for all aging conditions is plotted in Figure 2d. 20% pre-deformation this strain-shift ($\Delta\varepsilon$) was low (0.1%), while after 50% of pre-deformation the shift was higher (2.6%). Aging additionally affects this strain-shift, thus the highest $\Delta\varepsilon$ was found after 50% pre-deformation and 5 days of aging (3.7%). The work hardening is almost unaffected by aging and did not affect the TE after 20% of pre-deformation. After 50% pre-deformation, the TE decreases with increasing aging time (23.8% → 20.8% → 17.9%).

The static strain aging was analyzed by SANS, which enabled the identification of the size and number density of short-range ordered regions (**Figure 3**). Pre-deformation and aging led to a

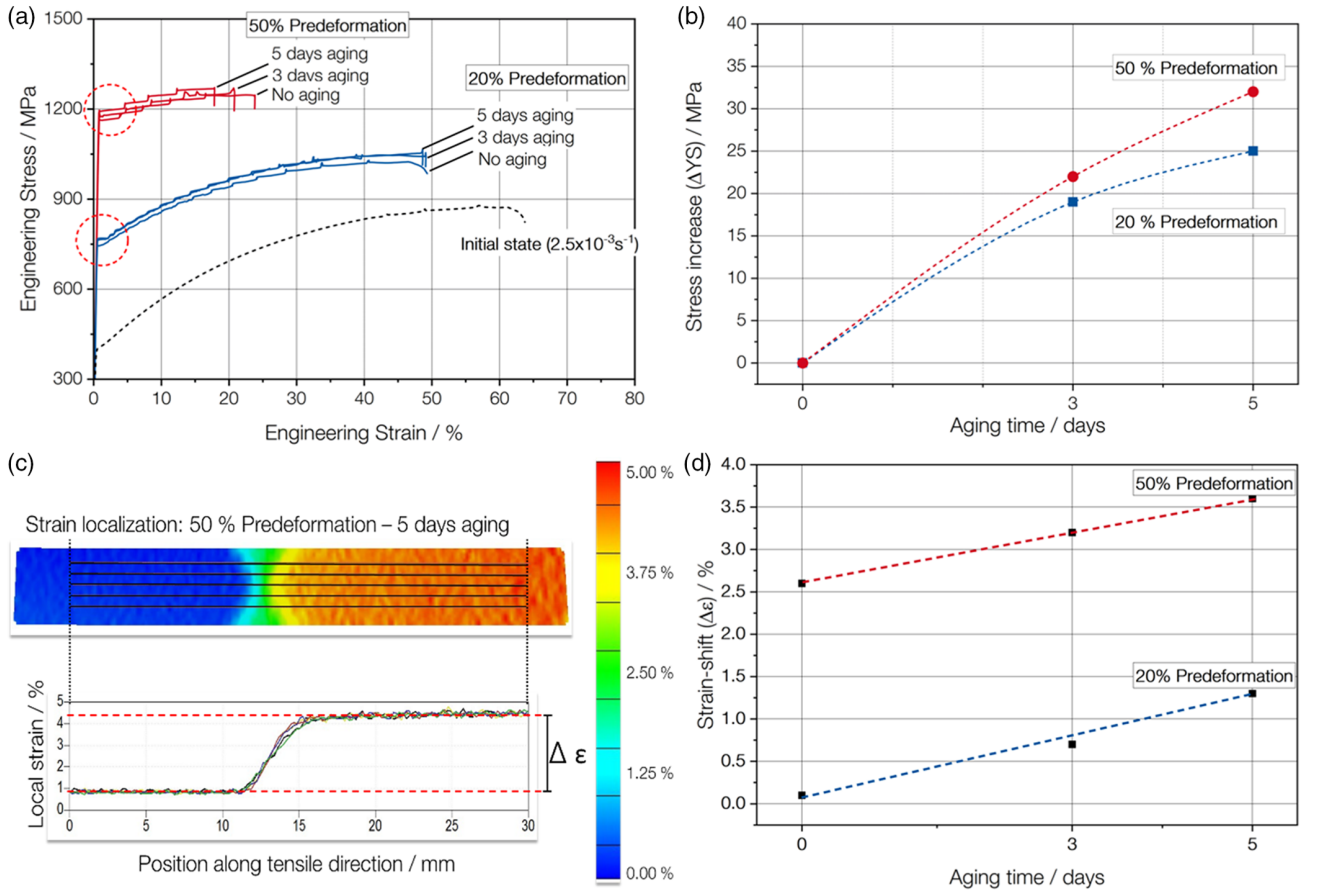

Figure 2. a) Stress–strain curves of the initial state and after 20% and 50% pre-deformation and aging; b) Stress increase due to aging after prestaining; c) Local distribution of strain along x-axis during pronounced yielding from digital image correlation after 50% pre-deformation and 5 days of aging and depiction of strain increase $\Delta\varepsilon$; d) Strain-shift during pronounced yielding from strain localization as shown in (c).

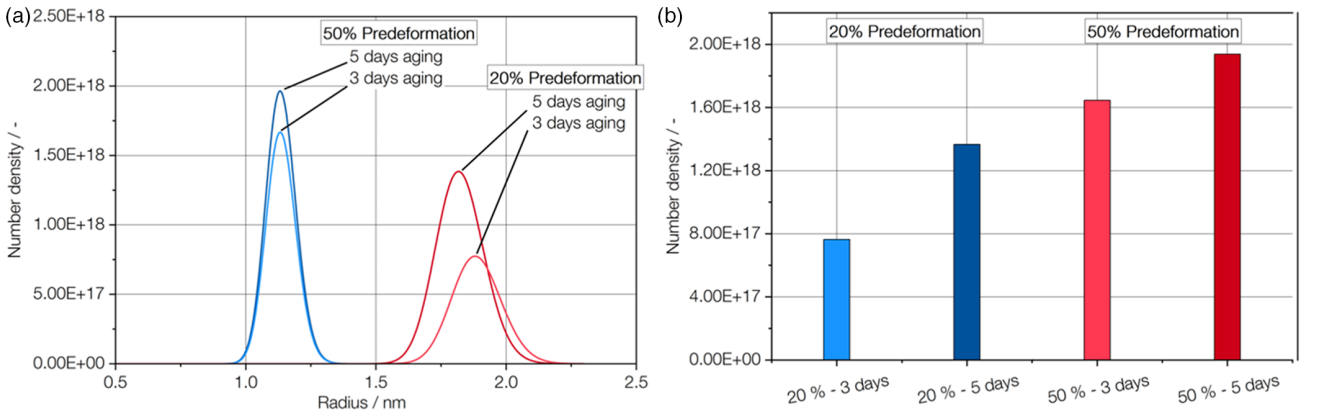

Figure 3. a) SANS results of the samples for different pre-deformation and aging times. b) Number density of the C–Mn-ordered clusters at different deformation and aging states.

high number density of C–Mn-ordered clusters in the order of 10^{18}. As shown in Figure 3a, a higher degree of pre-deformation, i.e., 50% pre-deformation, led to an even higher number density and smaller size of the clusters. As shown in Figure 3b, the number density of C–Mn-ordered clusters increased with aging time. After 20 % of deformation, aging resulted in a number density of 0.76×10^{18} and 1.37×10^{18} after 3 and 5 days, respectively. 50% of pre-deformation increased the number density after 3 and 5 days to 1.64×10^{18} and 1.94×10^{18}, respectively.

4. Discussion

The experimental results of the investigated austenitic high-manganese steel show a strong impact of aging on the mechanical properties (Figure 1 and 2) as well as on C–Mn ordering at nanoscale (Figure 3).

Our results show that shorter dynamic strain-aging, as from higher strain rate, resulted in a decrease in total strength, but does not affect the YS. The lack of effect on YS is likely due to the fact that plastic strain is an essential precondition for strain aging.[30] The results show a change in total strength, which is a typical effect in high manganese steels and is accommodated by a negative strain rate sensitivity and a serrated flow.[38–41] As some of the tensile samples were tested at strain rates above $10^{-3}\,s^{-1}$, we expect them to experience adiabatic heating as other authors have shown for austenitic steels.[42,43] The higher temperature, which occurs after some plastic deformation, accelerates diffusive processes like aging. Although, we, as well as other authors, found that the increasing temperature leads to lower tensile strength, reduces strain hardening, and retards the onset of serrated flow.[39,44,45] However, at higher strain rates, several effects could occur simultaneously in addition to strain aging, making it hard to correlate our findings. For example, the tendency to planar slip is reduced, which reduces the formation of twins. The effects during dynamic strain aging make it difficult to assign the reasons for lower strength and later onset of serrated flow.[46,47]

Static strain aging was investigated by interrupted tensile tests conducted at a constant strain rate of $2.5 \times 10^{-3}\,s^{-1}$. To analyze the processes of the nanostructure during static aging, the samples were examined with SANS additionally. The increase in YS, as known from other high-manganese steels, occurs due to strain aging.[40,48] The increase in YS is repeatedly attributed to the hindrance of the dislocation movement or a combined effect of ordering and dislocation hindering.[49–51] We found that the strength increase intensifies with longer aging times and higher pre-deformation (Figure 2b). A higher pre-deformation comes along with a higher dislocation density, which as well increases the probability for the displacement of carbon atoms on tetrahedral interstitial sites during straining.[52] Subsequent aging leads to a reorientation, which is argued to influence dislocation movement and thus would lead to a strength increase.[9] This is a possible explanation, why pre-deformation and aging duration are related to strength increase.

In addition, we found a stronger localization of plastic strain with higher increase in YS. The plastic deformation localizes and a Lüders-band-like strain-shift occurs at the beginning of the plastic flow. Digital image correlation shows that the localization of plastic deformation is starting in the sample shoulders and moving along the parallel length of the sample. Reasons for localization probably have the same origin as localization during serrated flow and are still a matter of conjecture. Some authors state that dislocation and twin substructures responsible for the localization of strain.[53,54] Others point out that the interactions from C–Mn complexes are reasonable.[12,55] A combination of short-range ordering and twinning is stated by Sevsek et al. to be responsible for a serrated flow.[49] Even if none of the causes for localization of the strain is clear, our results show a clear relationship between the increase in stress, the intensity of the serrated flow, and the formation of a short-range order.

Our results show that aging continues after deformation even at room temperature. Other studies used SANS as well but did not take aging at room temperature into account or accounted for the increase in the number density of C–Mn complexes solely to straining.[56] The influence of aging is accelerated by straining and the higher dislocation density. The increasing strength and the intensified strain-shift are accommodated by an increased number of C–Mn-ordered clusters that arise during aging at room temperature. The analysis from SANS correlates a stronger pronounced yielding and a higher YS with a higher number of C–Mn complexes (Figure 3), which would suggest a causal relationship between strain aging and ordering. This is in agreement with some authors, stating ordering as the origin of strain aging in high-manganese steels.[12,33,49] Others, assume cluster formation is impossible, as they state the time needed to form C–Mn clusters is up to 10^{27} s.[57] A combined effect is stated to increase planar slip due to short-range ordering and thus increase twinning, which would as well explain the stronger localization [37,58,59] as twinning promotes a serrated flow.[20,60,61] Other investigations even show that not only does a higher pre-deformation intensifies strain aging, but also an increase in temperature or a higher strain rate during pre-deformation further accelerates the static strain aging process.[40,48]

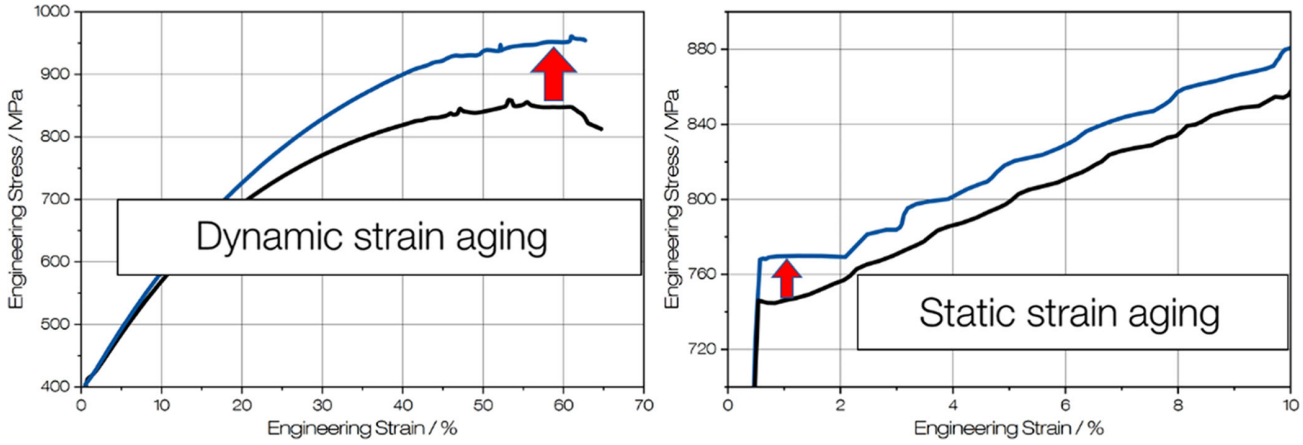

Figure 4. Impact of dynamic and static strain aging on mechanical properties.

Even though our results show a correlation between C–Mn ordering and strength increase during static strain aging, this cannot be equally assumed for dynamic strain aging. This important aspect becomes apparent in the comparison of strain localization. During static strain aging, a clear increase in localization occurs after a longer aging time. During dynamic strain aging, no strain rate-dependent variance in the strength of the localization can be identified. Nevertheless, the findings show that dynamic as well as static strain aging increase the necessary stresses for plastic deformation as depicted in **Figure 4**. Static strain aging increases the general strength level, dynamic strain aging affects the strain hardening during the tensile test.

5. Conclusions

The static and dynamic strain aging of high-manganese steel (Fe-22Mn-1.3Al-0.3C) has been investigated. The main conclusions are as follows: 1) A higher strain rate leads to an earlier onset of serrated flow during plastic deformation. However, this dependence is only valid until a strain rate of 10^{-3} is reached and adiabatic heating is expected. 2) Static strain aging caused a pronounced yielding phenomenon in the investigated high manganese steel. Aging is influenced by the pre-deformation and aging time. Both higher pre-deformation and longer aging time do not only increase the YS, but also increase the localization of strain during pronounced yielding. 3) The observed aging phenomena are most probably related to C–Mn ordering. The microstructural regions affected by C–Mn ordering were quantified from SANS data.

Acknowledgements

The authors gratefully acknowledge the financial support of the DFG (Deutsche Forschungsgemeinschaft) within the collaborative research center SFB 761 "steel – ab initio." In addition, the authors want to thank Nima Babaei, Marion Kreins, and Daniela Wipp for their expertise and fruitful discussions throughout all aspects of our study.

Open access funding enabled and organized by Projekt DEAL.

Conflict of Interest

The authors declare no conflict of interest.

Data Availability Statement

The data that support the findings of this study are available on request from the corresponding author. The data are not publicly available due to privacy or ethical restrictions.

Keywords

C–Mn ordering, deformation behavior, high-manganese steel, small-angle neutron scattering, strain aging

Received: November 3, 2021
Revised: February 2, 2022
Published online:

[1] G. Frommeyer, U. Brüx, P. Neumann, *ISIJ Int.* **2003**, *43*, 438.
[2] M. Bambach, L. Conrads, M. Daamen, O. Güvenç, G. Hirt, *Mater. Des.* **2016**, *110*, 157.
[3] S. Wesselmecking, M. Kreins, M. Dahmen, W. Bleck, *Mater. Des.* **2022**, *213*, 110357.
[4] J.-H. Schmitt, T. Iung, *C. R. Phys.* **2018**, *19*, 641.
[5] W. Bleck, *Int. J. Miner. Metall. Mater.* **2021**, *28*, 782.
[6] S. Wesselmecking, M. Haupt, Y. Ma, W. Song, G. Hirt, W. Bleck, *Mater. Sci. Eng.: A* **2021**, *828*, 142056.
[7] G. Yang, J.-K. Kim, *Metals* **2021**, *11*, 124.
[8] W. Song, T. Ingendahl, W. Bleck, *Acta Metall. Sin.* **2014**, *27*, 546.
[9] S.-I. Lee, S.-Y. Lee, J. Han, B. Hwang, *Mater. Sci. Eng.: A* **2019**, *742*, 334.
[10] Essoussi, H., Ettaqi, S., E. H. Essadiqi, *Procedia Manuf.* **2018**, *22*, 129.
[11] H. Kim, D.-W. Suh, N. J. Kim, *Sci. Technol. Adv. Mater.* **2013**, *14*, 14205.
[12] S.-J. Lee, J. Kim, S. N. Kane, B. C. de Cooman, *Acta Mater.* **2011**, *59*, 6809.
[13] L. Samek, E. de Moor, J. Penning, J. G. Speer, B. C. de Cooman, *Metall. Mater. Trans. A* **2008**, *39*, 2542.
[14] S. Das, S. B. Singh, O. N. Mohanty, *Ironmaking Steelmaking* **2011**, *38*, 139.
[15] H. K. D. H. Bhadeshia, *J. Mater. Sci.* **2004**, *39*, 3949.
[16] J.-K. Kim, B. C. De Cooman, *Steel Research Int.* **2009**, *2009*, 493.
[17] K. Renard, S. Ryelandt, P. J. Jacques, *Mater. Sci. Eng.: A* **2010**, *527*, 2969.
[18] U. F. Kocks, R. E. Cook, R. A. Mulford, *Acta Metall.* **1985**, *33*, 623.
[19] R. A. Mulford, U. F. Kocks, *Acta Metall.* **1979**, *27*, 1125.
[20] X. Bian, F. Yuan, X. Wu, *Mater. Sci. Eng.: A* **2017**, *696*, 220.
[21] P. Larour, A. Bäumer, K. Dahmen, W. Bleck, *Steel Research Int.* **2013**, *84*, 426.
[22] J.-K. Kim, L. Chen, H.-S. Kim, S.-K. Kim, G. S. Kim, Y. Estrin, B. C. DeCooman, *Mater. Technol.* **2009**, *493–498*.
[23] A. H. Cottrell, *Lond. Edinburgh Dublin Philos. Mag. J. Sci.* **1953**, *44*, 829.
[24] J. S. Koehler, *Science (New York, N.Y.)* **1953**, *119*, 551.
[25] A. V. Nazarov, A. A. Mikheev, *J. Phys.: Condens. Matter* **2008**, *20*, 485203.
[26] S.-J. Lee, D. K. Matlock, C. J. van Tyne, *ISIJ Int.* **2011**, *51*, 1903.
[27] D. E. Jiang, E. A. Carter, *Phys. Rev. B* **2003**, *67*, 214103.
[28] H. K. D. H. Bhadeshia, R. W. K. Honeycombe, *Steels: Microstructure and Properties*, Butterworth-Heinemann c/o Elsevier, Oxford **2007**.
[29] P. Lan, J. Zhang, *Mater. Sci. Eng.: A* **2017**, *700*, 250.
[30] M. Koyama, T. Sawaguchi, K. Tsuzaki, *Tetsu to Hagane* **2018**, *104*, 187.
[31] H. Tanimoto, *Newly Developed Method of Measurement for Conversion Electron Mossbauer Spectroscopy and its Applications in Material Sciences*, Osaka **1990**.
[32] J. von Appen, R. Dronskowski, *Steel Res. Int.* **2011**, *82*, 101.
[33] J.-H. Kang, T. Ingendahl, J. von Appen, R. Dronskowski, W. Bleck, *Mater. Sci. Eng.: A* **2014**, *614*, 122.
[34] M. Grujicic, W. S. Owen, *Calphad* **1992**, *16*, 291.
[35] T. Hickel, S. Sandlöbes, R. Marceau, A. Dick, I. Bleskov, J. Neugebauer, D. Raabe, *Acta Mater.* **2014**, *75*, 147.
[36] R. Xie, S. Lu, W. Li, Y. Tian, L. Vitos, *Acta Mater.* **2020**, *191*, 43.
[37] W. Song, D. Bogdanovski, A. Yildiz, J. Houston, R. Dronskowski, W. Bleck, *Metals* **2018**, *8*, 44.
[38] J. B. Seol, J. G. Kim, S. H. Na, C. G. Park, H. S. Kim, *Acta Mater.* **2017**, *131*, 187.
[39] M. Madivala, W. Bleck, *JOM* **2019**, *71*, 1291.
[40] M. Koyama, E. Akiyama, K. Tsuzaki, *ISIJ Int.* **2013**, *53*, 1089.
[41] M. Koyama, E. Akiyama, K. Tsuzaki, *Scr. Mater.* **2012**, *66*, 947.
[42] N. I. Vázquez-Fernández, T. Nyyssönen, M. Isakov, M. Hokka, V.-T. Kuokkala, *Acta Mater.* **2019**, *176*, 134.

[43] N. I. Vazquez-Fernandez, G. C. Soares, J. L. Smith, J. D. Seidt, M. Isakov, A. Gilat, V. T. Kuokkala, M. Hokka, *J. Dyn. Behav. Mater.* **2019**, *5*, 221.
[44] Y. F. Shen, N. Jia, R. Misra, L. Zuo, *Acta Mater.* **2016**, *103*, 229.
[45] R. Kapoor, S. Nemat-Nasser, *Mech. Mater.* **1998**, *27*, 1.
[46] O. A. Zambrano, *J. Eng. Mater. Technol.* **2016**, *138*, 41010.
[47] V. Gerold, H. P. Karnthaler, *Acta Metall.* **1989**, *37*, 2177.
[48] S. Wesselmecking, W. Song, Y. Ma, T. Roesler, H. Hofmann, W. Bleck, *Steel Res. Int.* **2018**, *89*, 1700515.
[49] S. Sevsek, F. Brasche, C. Haase, W. Bleck, *Mater. Sci. Eng.: A* **2019**, *746*, 434.
[50] S. Sevsek, W. Bleck, *Metals* **2018**, *8*, 34.
[51] J.-H. Kang, T. Ingendahl, W. Bleck, *Mater. Des.* **2015**, *119*, 340.
[52] B. Hutchinson, N. Ridley, *Scr. Mater.* **2006**, *55*, 299.
[53] I. Gutierrez-Urrutia, D. Raabe, *Acta Mater.* **2011**, *59*, 6449.
[54] S. D. Antolovich, R. W. Armstrong, *Progr. Mater. Sci.* **2014**, *59*, 1.
[55] S. Hong, S. Y. Shin, J. Lee, D.-H. Ahn, H. S. Kim, S.-K. Kim, K.-G. Chin, S. Lee, *Metall. Mater. Trans. A* **2014**, *45*, 633.
[56] M. Kang, E. Shin, W. Woo, Y.-K. Lee, *Mater. Charact.* **2014**, *96*, 40.
[57] S.-K. Oh, M. E. Kilic, J.-B. Seol, J.-S. Hong, A. Soon, Y.-K. Lee, *Acta Mater.* **2020**, *188*, 366.
[58] M. Koyama, T. Sawaguchi, K. Tsuzaki, *ISIJ Int.* **2015**, *55*, 1754.
[59] V. Shterner, I. B. Timokhina, H. Beladi, *AMR* **2014**, *922*, 676.
[60] X.-J. Wang, X.-J. Sun, C. Song, H. Chen, S. Tong, W. Han, F. Pan, *Acta Metall. Sin. (Engl. Lett.)* **2019**, *32*, 746.
[61] T. A. Lebedkina, M. A. Lebyodkin, J.-P. Chateau, A. Jacques, S. Allain, *Mater. Sci. Eng.: A* **2009**, *519*, 147.